Electronic Supplementary Material (ESI) for Journal of Materials Chemistry B.

SUPPORTING INFORMATION

Flexible, Ultra-Sensitive Chemical Sensor with 3D Biomimetic Templating for Diabetes-Related Acetone Detection

Lili Wang,[a,c] Joshua A. Jackman,[a] Jae Hyeon Park,[a] Ee-Lin Tan,[a] and Nam-Joon Cho*[,a,b]

[a]School of Materials Science and Engineering, Nanyang Technological University, 50 Nanyang Avenue, 639798 Singapore. E-mail: njcho@ntu.edu.sg

[b]School of Chemical and Biomedical Engineering, Nanyang Technological University, 62 Nanyang Drive, 637459 Singapore.

[c]State Key Laboratory on Integrated Optoelectronics, College of Electronic Science and Engineering, Jilin University, Changchun 130012, PR China

KEYWORDS: Chemical sensors; Biomimetic; Biological materials; Chemical detection; Fast Response, Porous materials

***Corresponding author**

Email: njcho@ntu.edu.sg

Methods

Materials: Potassium hydroxide solution (KOH), hydrochloric acid (HCl), ethanol (C_2H_5OH), acetic acid (CH_3COOH), hydrazine (N_2H_4, 35wt%), acetone (C_3H_6O), toluene (C_7H_8), and methanol (CH_3OH) were purchased from Alfa Aesar. Chitosan (medium molecular weight) and graphene oxide (GO, > 95%) were purchased from Sigma-Aldrich. Silver paste (CW2900) was purchased from Chemtronics (US). Advantec cellulose papers were purchased from Toyo Roshi Kaisha, Ltd (Japan). Copper Tape-Copper Foil was purchased from Rapid Electronics Ltd (UK). All commercially available chemicals were used as received.

Preparation of Chitosan. Natural chitosan was extracted from Knight butterfly wings by a series of chemical methods followed by deacetylation of chitin as outlined in supporting information Fig. S1.48 First, raw butterfly wings were dipped in 20 mL of ethanol for 15 min followed by a thorough rinse with 3% HCl. Subsequently, the wings were soaked in 5% KOH solution for 5 min and rinsed with ethanol. The specific preparation steps were performed to ensure effective removal of mineral constituents, proteins, and pigments from the surface of the material. Finally, deacetylation of chitin was achieved by KOH alkalinization in which a 30 min incubation in 40% KOH heated at 40 °C would transform the chitin into chitosan.

Preparation of rGO-coated three-dimensional chitosan (3D CS@rGO): The extracted chitosan was flattened on a glass culture dish and then was incubated for 1 hour on an orbital shaker (Heidolph unimax 1010) set at 100 rpm while immersed in 20 mL of GO solution that had been prepared at a 50-fold dilution from stock (0.04 mg mL^{-1}) with aqueous solution (50 v/v%, ethanol and water). After 1 h, 0.6 mL of hydrazine

(35 wt%) was injected into the solution and incubated under continuous agitation for an extra 2 h to obtain the reduced form of graphene oxide (rGO). Finally, 3D CS@rGO was isolated from the solution under mild suction filtration with water

Preparation of rGO-coated bulk chitosan (Bulk CS@rGO) and rGO-coated no structure chitosan (no-structure CS@rGO): 0.1 g of CS powder was suspended in 20 mL of GO solution containing a 1:1 mixture of GO stock solution and acetic acid and was stirred overnight. The next day, 0.6 mL hydrazine (35wt%) was added in to the solution to reduce the GO and was incubated with continued stirring for two more hours. The bulk CS@rGO was obtained by freeze drying samples were obtained by freeze drying (Labconco, FreeZone-738606) while no-structure CS@rGO was isolated on a cellulose paper via air evaporation. The final samples were rinsed with water several times over a filter paper.

Sample characterization. Field Emission Scanning Electron Microscope (FESEM, JEOL-6340F, Japan) was operated at 10 kV to examine the surface morphology of the samples. The Raman spectra of the butterfly wing and CS@rGO were acquired using a confocal Raman microscope (WITec, Ulm, Germany) with a 488 nm laser excitation, a spatial resolution of 1 μm, and an accumulation time of 3 s at each spot. Each measurements were performed in triplicates and the representative data were reported. X-ray diffraction (XRD) patterns were obtained from the X-ray diffractometer (XRD-600, Shimadzu, Japan) in the range of 5-50° (2θ) at a scanning rate of 3° min^{-1}. Atomic force microscope (AFM, NX-Bio, Park Systems, Suwon, South Korea) was implemented to obtain scanning ion conductance microscopy (SICM) images using a silicon cantilever operating at a non-contact tapping-force mode. The fourier transform infrared

spectroscopy (FTIR) was recorded on a Thermo Fisher Nicolet 6700 spectrometer. Hydrophilicity/hydrophobicity was investigated by monitoring the deposit angle of water droplets (approximately 2 µL) deposited on the material surfaces using Attension Theta Optical Tensiometer (Biolin Scientific Holding AB, Sweden) with OneAttension 1.0 software (10 s at 12 FPS). Optical microscopy images were obtained using an Olympus inverted microscope with a bright field condenser which were recorded with a digital camera (600D, Canon, Japan) and colored-images were collected using Photometrics CoolSNAP-cf cooled CCD camera.

Flexible sensor device assembly. A conventional two-electrode system was adopted as detailed in Fig. S6a. The electrodes (copper foil) are in contact with the CS@rGO/cellulose paper (1.5 cm × 0.5 cm), with a 1.0 cm separation between the two electrodes for all experiments. For both ends, Cu wires were fixed in between the sensing layer and Cu electrodes using silver paste. The electrical current measurements were collected with Keithley multimeter (DMM-7510) and digital multimeter (BK precision 2709 B tool KIT).

Vapor collection and measurement. The gas vapors were obtained from corresponding liquid, and vapor concentrations (C) were calculated with the following equation:

$$Q = \frac{1}{22.4 \times 10^6} \frac{VCM}{d\rho} \frac{273 + T_R}{273 + T_R}$$

where Q is the liquid volume, V is the volume of the glass chamber, M is the molecular weight of the liquid, and C is the target gas concentration. The volume fraction and specific gravity of the liquid is represented as d and ρ, respectively, and TR and TB are

the temperatures inside and outside of the glass chamber. To simulate diabetic breath, exhaled breath samples from healthy non-smoker volunteers were collected in bags with added acetone vapors.[1,2] From this method, the relative humidity value of exhaled breath was measured to be approximately 85%RH using the Multifunctional Hygrometer MC20.

Vapor sensor performance evaluations. The assembled vapor sensor was integrated into a home-made testing equipment for performance evaluations (Fig. S6b). The sensors were placed in a tube supported by a PDMS substrate layer and the fluctuation in sensor resistance in response to change in atmosphere was monitored with a Keithley 2636b System SourceMeter (Keithley). For p-type sensing layer, sensitivity (S) of sensors were defined as:

$$\mathrm{S}\ (\%) = \frac{\mathrm{R} - R_0}{R_0} \times 100$$

Where R0 represents the initial resistance in air and R represents the measured resistance in vapor sample. The time required for the sensor to achieve 90% maximum was defined as its response time (T_{r1}) and the opposite to be defined as the recovery time (T_{r2}).[3]

Supplementary Discussion

Design, synthesis and sensing properties of the CT@rGO composites. (Fig. 5). To further prove the distinctive capability of chitosan, we used identical methods to prepare CT@rGO composites (see Methods and Fig. 5a) and investigated the acetone vapors sensing properties. Fig. S5a illustrates a schematic of the fabrication procedure and the chemical structures of the samples for the synthesized CT@rGO biocomposite. However, natural chitin contains less amino groups (approximately 5%-15%)[4] and is generally considered insoluble [5] when compared to chitosan, thus, the surface-coating of graphene oxide on chitin is considered random and weakly interacting (Fig. S5b). This result can be further observed through FESEM and AFM analyses depicting random distribution of rGO nanosheet over the surface of the chitin-based material (Figs. S5c-d). The texture-less flat area between the obvious ridges are indicative of minimal or negligible association of rGO to the CT substrate. Such weak interaction not only reduces the electrical conductivity, but is expected to minimize the mass\electrical transport properties. Indeed, the significantly less conductivity can be observed from the 3D CT@rGO compared to that of the 3D CS@rGO as expected (Fig. S5e). Concomitantly, the acetone vapor sensitivity of the 3D CT@rGO-based sensor is also less than that of the 3D CS@rGO-based sensor (Fig. S5f).

Bulk/non-structured CS@rGO–based sensor (Fig. S7-8). Biomimetic and artificial (bulk and non-structured) CS@rGO was explored in parallel for the vapor sensor application (see Methods). As displayed in Fig. 3e of the main text and Fig. S8, 3D CS@rGO is characterized with a periodic hierarchical nanostructure, which maximizes the porosity and hence the permeability, offering unique physicochemical properties and

functions that are both highly desirable and markedly advantageous for chemical sensors.[6] The natural 3D structure grants an enhanced surface effectivity for acetone absorption but also increases the capacity of acetone vapors which drastically improves response rate in sensor applications. When directly comparing the performance of the sensors with different base structures (Fig. S7 and S8), the sensitivity of 3D CS@rGO to 5 ppm of acetone was calculated to be 34.8%, which is approximately 2.5-4.0 times greater than the bulk structured (14.5%) and no-structure (8.9%) sensors. However, the 3D CS@rGO sensor demonstrated similar limit of detection recording an approximate 1.2% at 50 ppb (Fig. 3f), which is comparable to the bulk CS@rGO (1.7% at 50 ppb) but still better than the no-structure CS@rGO (1.4% at 500 ppb) (Fig. S8). Nonetheless, the response and recovery time of the 3D structured sensor exhibited superior performance levels compared to the other devices (Fig. 3f).

Detailed detection of the 3D CS@rGO–based sensor to simulated exhaled breath (Fig. 9). The environmental humidity factors are important in the actual exhalant measurement.[7] In our experiment, freshly exhaled human breath reported RH value of nearly 100% (Multifunctional Hygrometer, MC20), while simulated diabetic breath (see Methods), reported an error of approximately 10%-15%RH. Therefore, to take in consideration the effect of the environmental factor, sensor sensitivity was tested on an artificially controlled RH setting (see Methods). Remarkably, by compared simulated and actual breath gas, the sensitivity of 3D CS@rGO–based sensor to humidity is similar (Fig. S9a). Fig. S9b shows the curve of sensor sensitivity to acetone at various RH settings. To eliminate the influence of the humidity on the chemical sensor, the humidity compensation experiments (Fig. S9c) were performed using the 3D sensor to

four concentration of acetone vapors at different humidity state. The sensor show good linearity on the whole, and still exhibits similar sensitivity through humidity, which is indicated that the humidity compensation is necessary to allows for accurate and consistent readings.

Detailed data and discussion on mechanical and sensing properties of flexible sensor. (Fig. S10-13). In Fig. 5b of main text and Fig. S10, the simulated diabetic-related acetone vapor was tested on the 3D CS@rGO sensor while under physical stress. With increased bending to the device, the sensitivity of sensor show no obvious deterioration maintaining the quick response and recovery to acetone vapor. We further challenged the bending and corresponding sensing properties of the 3D CS@rGO sensor as shown in Fig. 3f-h and Fig. S12. The resistance of the sensor showed negligible changes upon decisive bending and repetitive bending (Fig. 3g-h). Fig. S13 demonstrates the response/recovery curve of the sensor to 50 ppb of acetone vapors when bent at large angles (sudden bending, 85%RH). The rapid response and excellent reversibility of the sensor were fully retained even at large bending angles. The robustness of the paper-based gas sensor with respect to repeated bending is further demonstrated as seen in Fig. S12. The device shows only a slight decrease in resistance (about 17%) when subjected to 5 or 10-times bending cycles. Field Emission Scanning Electron Microscope (FESEM) analysis reveals some morphological wear due to the mechanical bending but overall preserve in structure (Fig. S11 and Fig. S12a-c).

Fully exposed wearable sensor application (Fig. 14). Real-time physiological monitoring was performed on a during a constant-load exercise. The accuracy of on-body measurements was verified through the comparison of on-body sensor

measurements while attached to the subject's wrist via in-situ (open chamber) and ex-situ (close chamber) measurements with simulated diabetic breath (Fig. 14). Decreases sensitivity is expected for the in-situ measurement owing to the open exposure to air, nonetheless, a limit of detection of 0.02 ppm (1.2%) was recorded, which is significantly less than the clinical (1.8 ppm).[8]

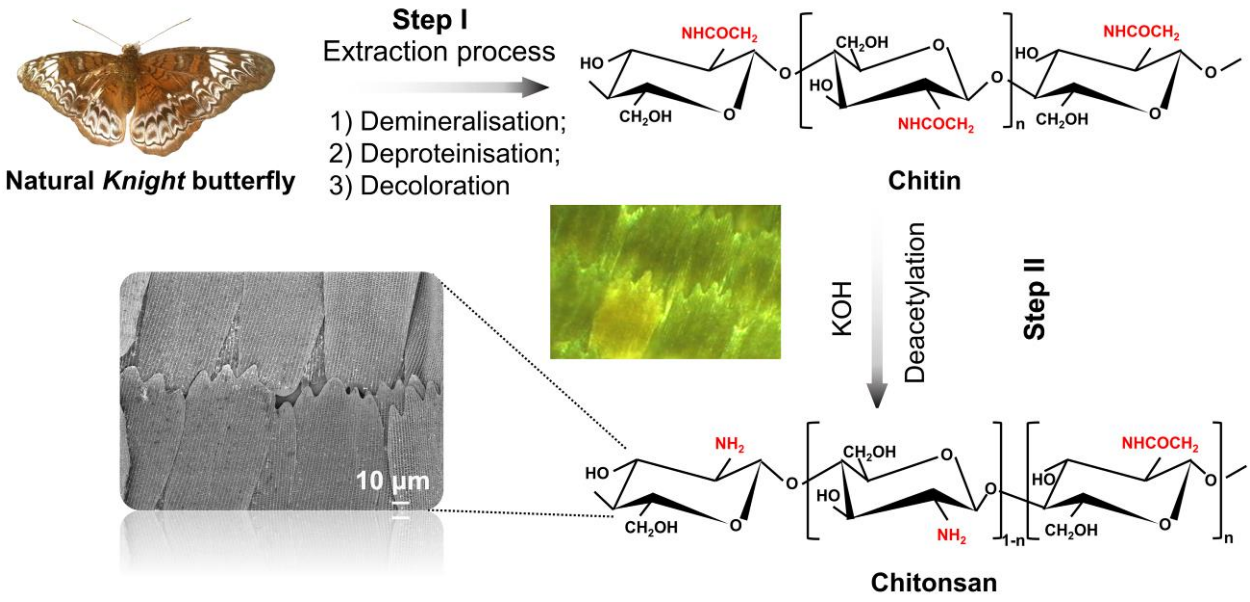

Fig. S1. Schematics of chitosan extraction from natural Knight Butterfly wings including chemical extraction and deacetylation. Step I: chitin extraction from butterfly wing by chemical methods; Step II: deacetylation of chitin to produce chitosan.

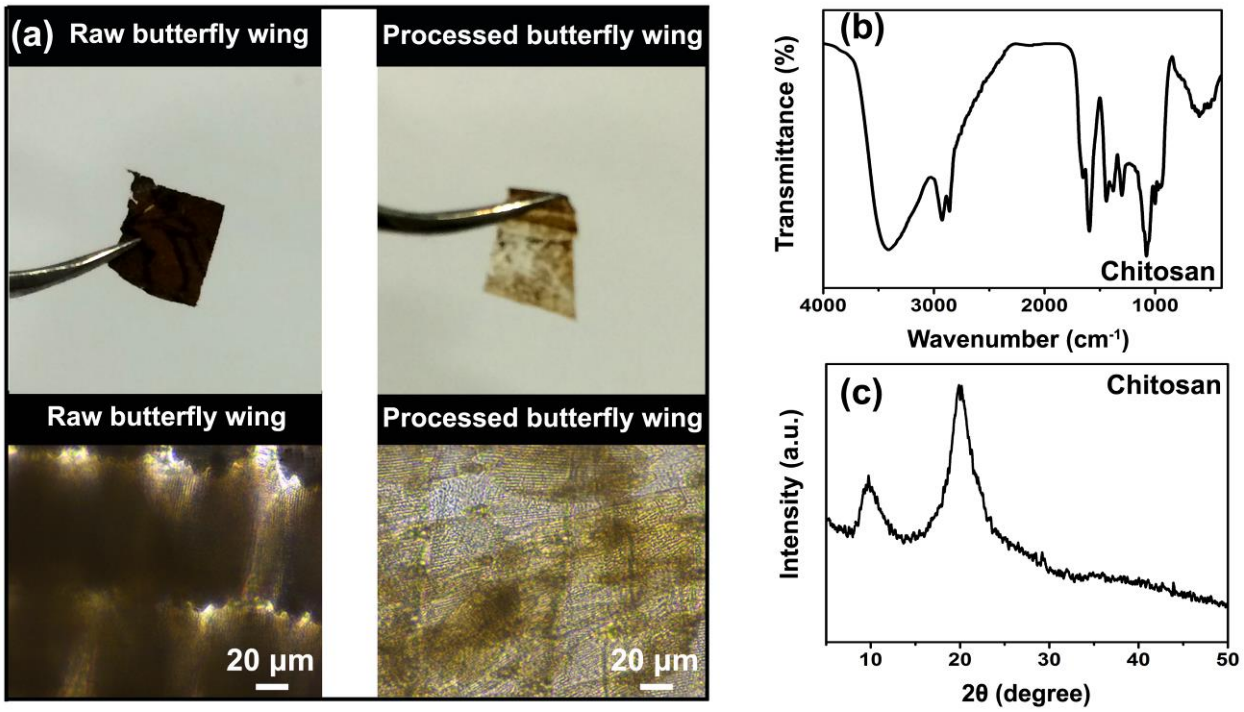

Fig. S2. Characterization of Knight butterfly wing. (a) Images of Knight butterfly wing before and after processing with raw sample fragment (top) and surface morphology observed by using optical microscopy (bottom). (b) FTIR spectroscopy of CS. (c) XRD pattern of CS.

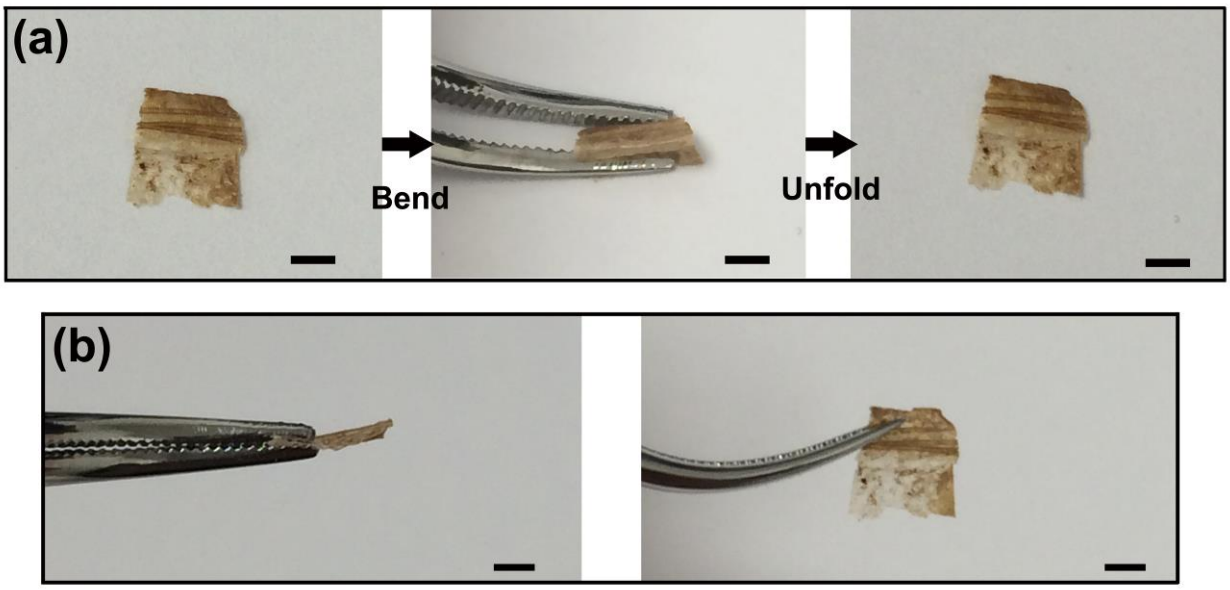

Fig. S3. Flexibility of natural CS biomaterials. (a) Images of CS material collapsing with applied force and its recovery. (b) Side and front view of obtained CS biomaterial. Scale bar: 0.2 cm.

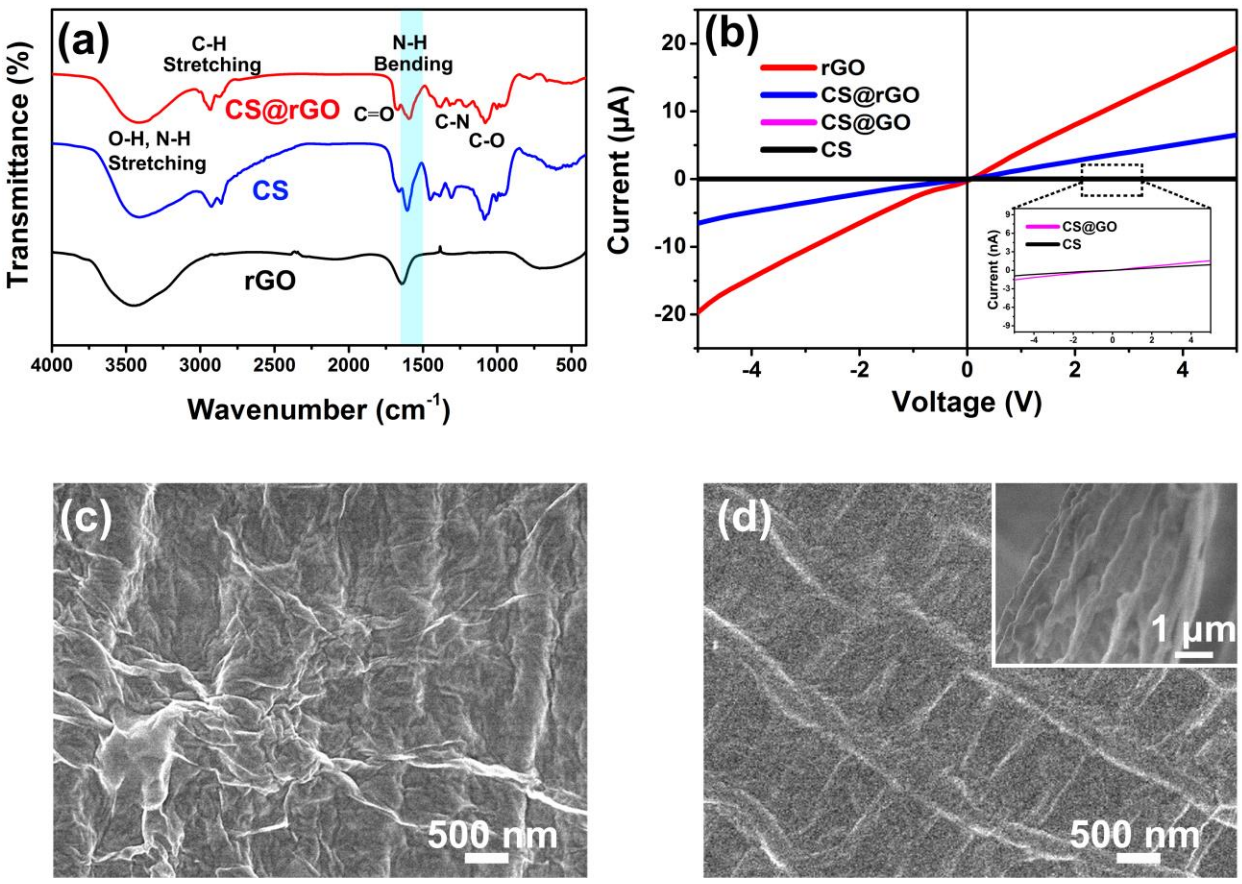

Fig. S4. Sample characterization. (a) FTIR spectroscopies of rGO, CS, and CS@rGO samples. (b) I-V curves of rGO, CS@rGO, and CS@rGO samples. The FESEM images of the biocomposite (c) before and (d) after treatment with hydrazine. Inset show the Cross-sectional SEM images of CS@rGO sample.

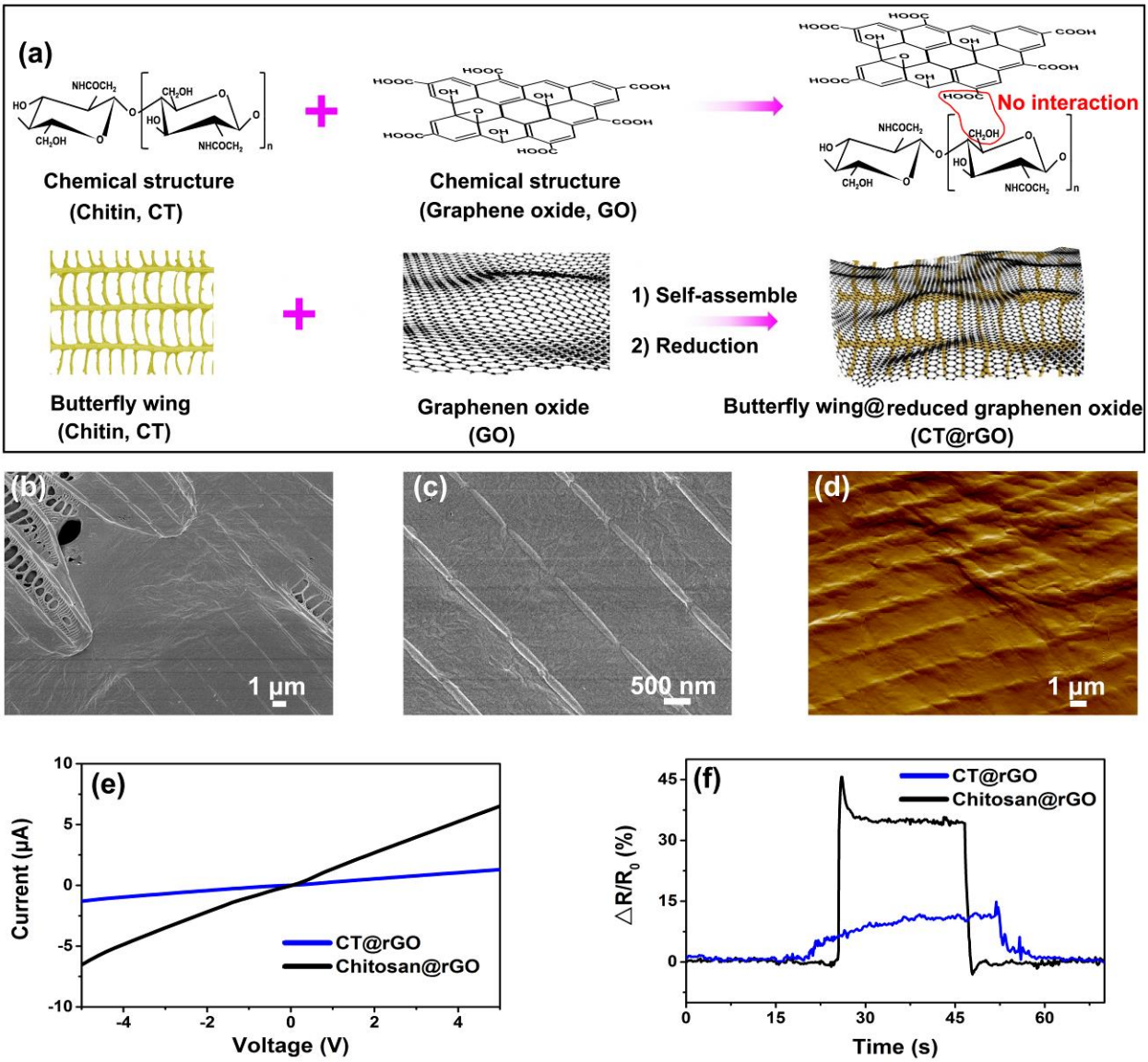

Fig. S5. Synthesis and characterization of CT@rGO. (a) Schematic diagram of the fabrication process of rGO-coated CT. Chemical structure of the materials are included to emphasize the absence of chemical interaction between the two. (b-c) FESEM images of CT@rGO. (d) AFM images of CT@rGO. (e) I-V curve of CT@rGO and CS@rGO. (f) Dynamic response curves of the CT@rGO-based and CS@rGO-based sensors to 5 ppm acetone vapors (1 cycle).

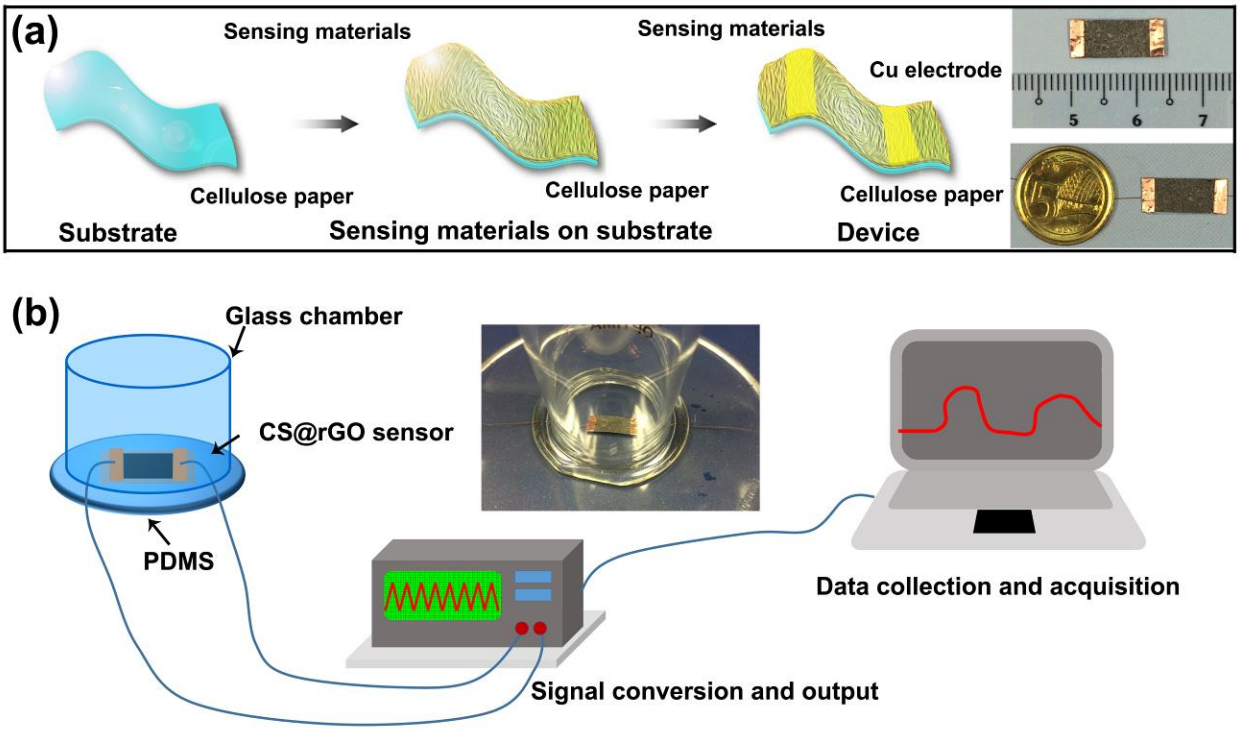

Fig. S6. Flexible vapor sensor device assembly and experiment platform. (a) Schematic representation of the sensor assembly (1.5 cm × 0.5 cm) including cellulose paper as the flexible bottom layer and rGO-coated biomaterial extracts as the sensing layer with Cu electrode strips at each end separated by 1.0 cm. (b) Schematic of the experimental setup and data collection method. Vapor samples are injected in a glass chamber supported by a PDMS layer and electrical fluctuations in the vapor sensor are measured by Kethley-2636B. Inset shows a photograph of experimental setup.

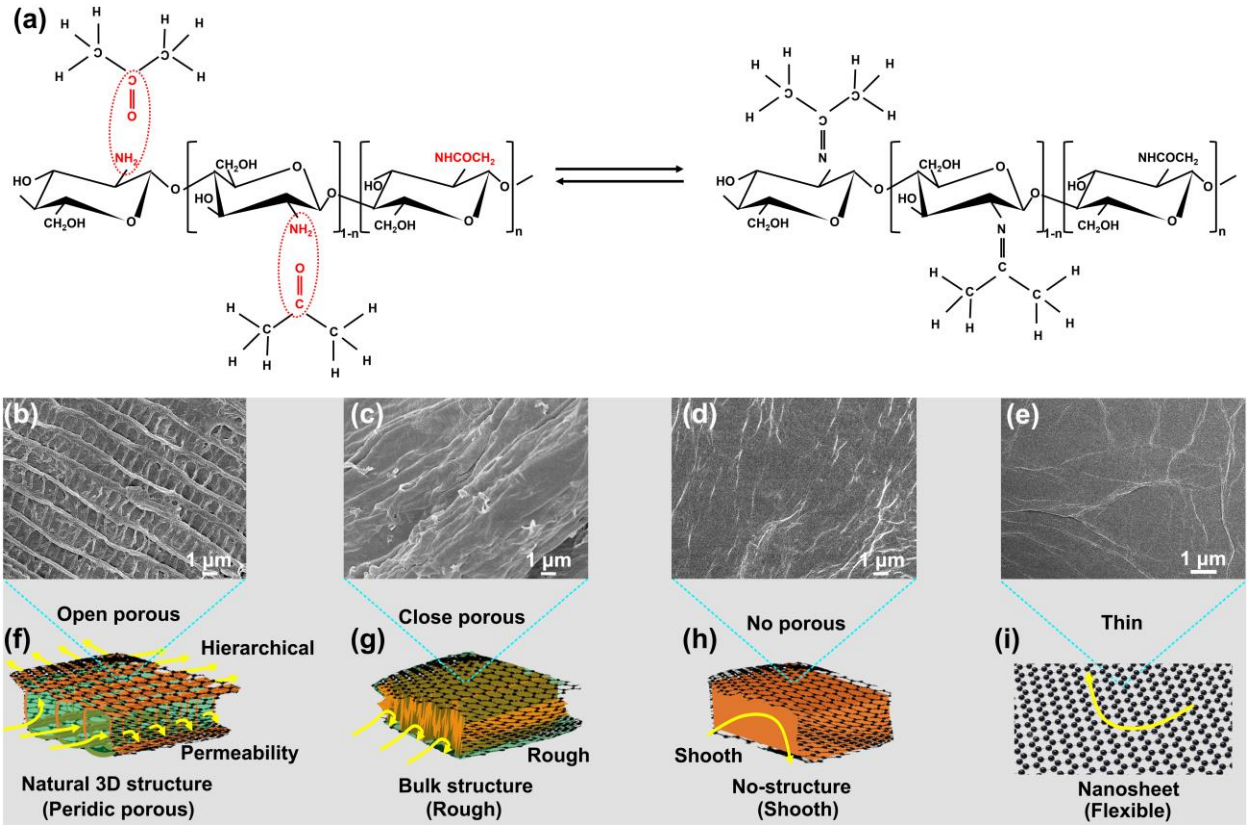

Fig. S7. Sensing principle of CS-based sensors. (a) Chemical reaction of CS@rGO with acetone molecules. (b-e) FESEM image of 3D CS@rGO, bulk CS@rGO, no-structure CS@rGO and pure rGO. (f-i) Prediction of sensor sensitivity depending on the corresponding structures of sensors.

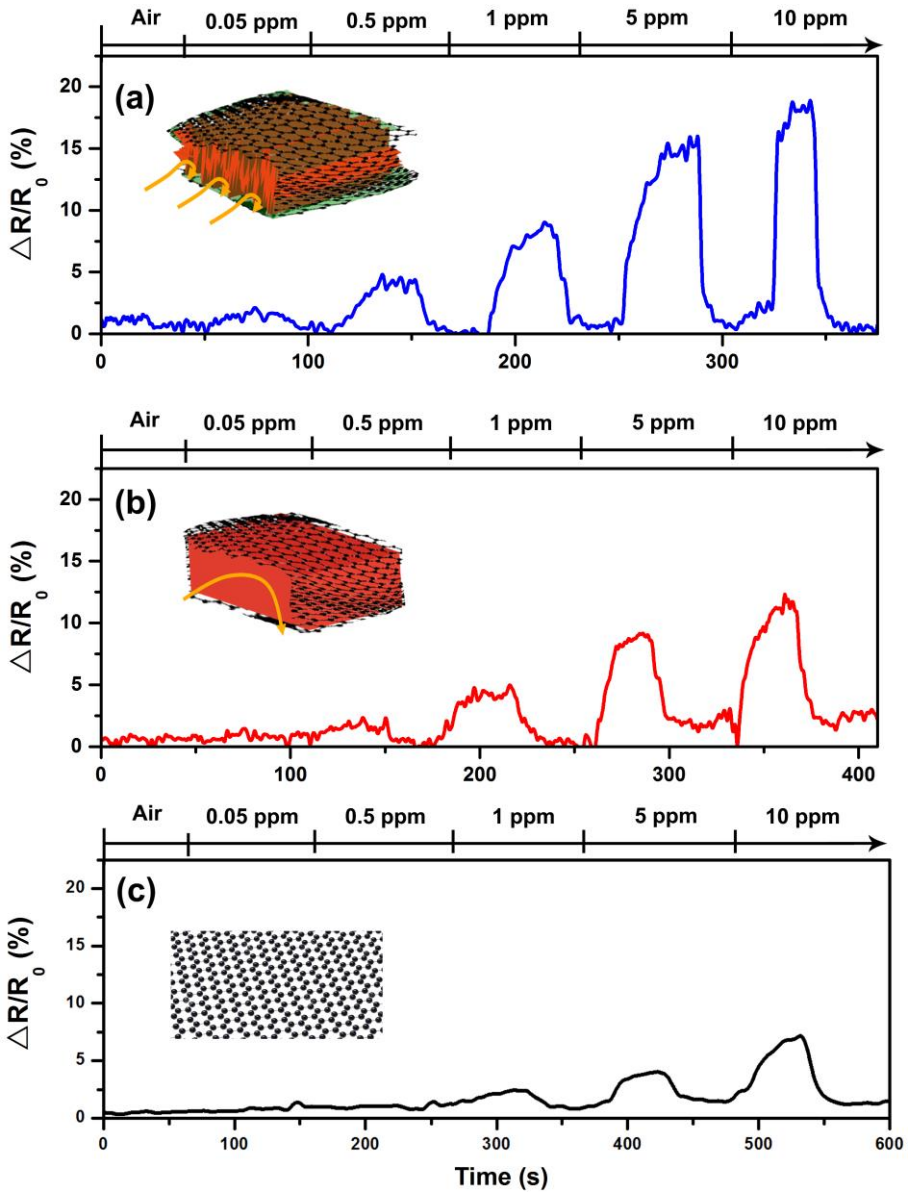

Fig. S8. Performance evaluations of the CS@rGO-based sensors. Change in relative resistance (%) with time in response to acetone vapors gradually increasing in concentration from 1 to 100 ppm (balanced in air). (a) Sensitivity of bulk CS@rGO, (b) sensitivity of no-structure CS@rGO, and (c) pure rGO.

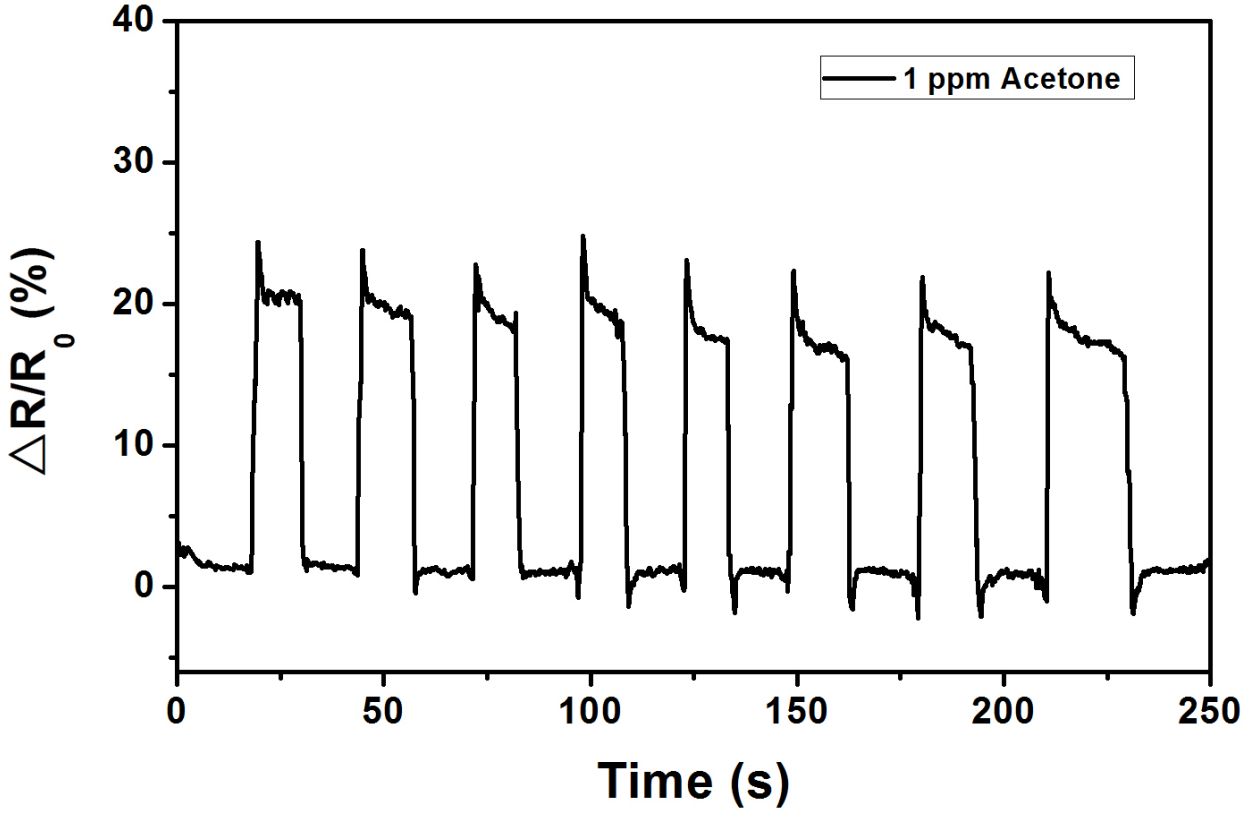

Fig. S9. The stability of the the CS@rGO-based sensors to 1 ppm acetone at room temperature.

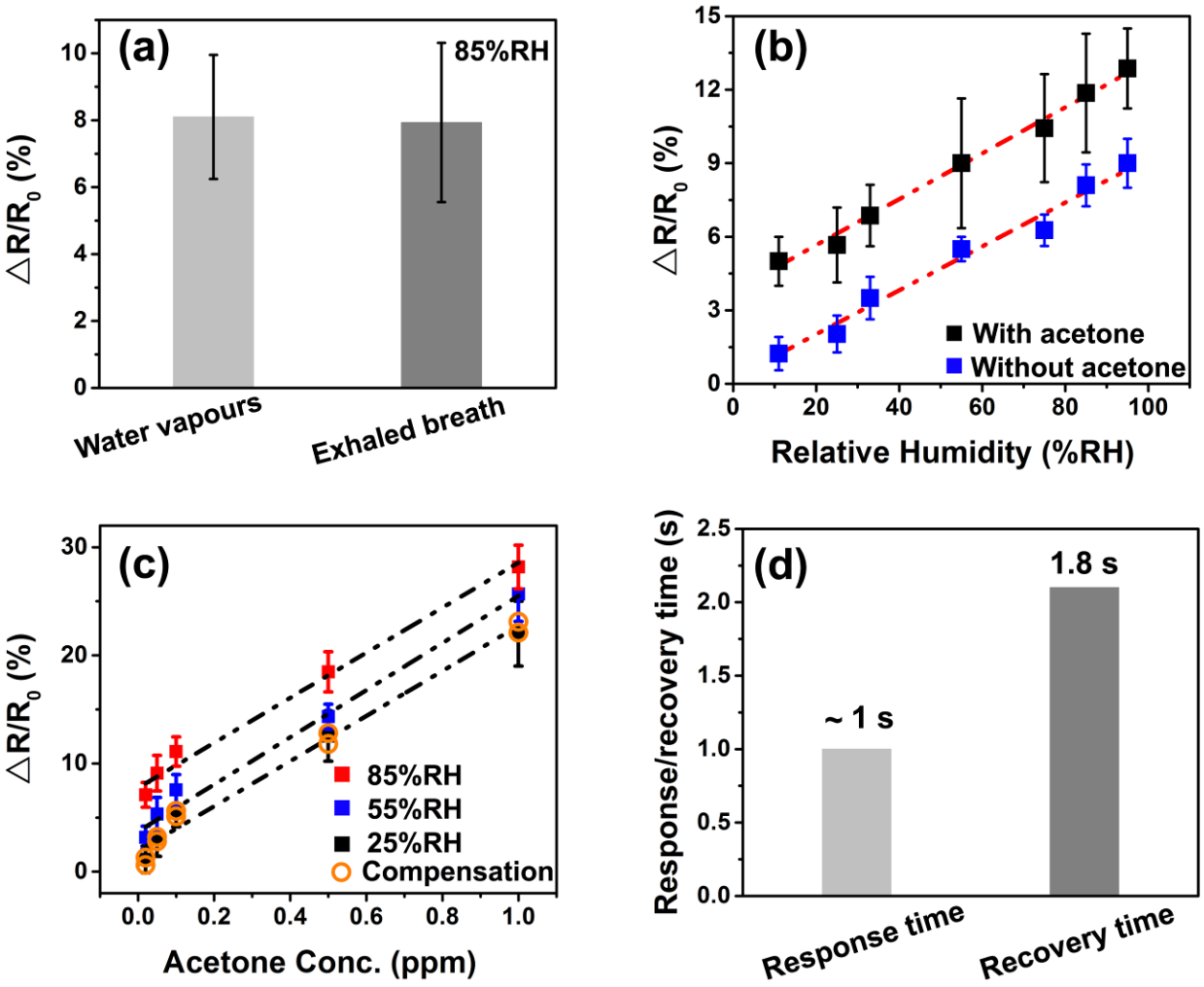

Fig. S10. Measurement of vapor samples using CS@rGO vapor sensor. (a) Measurement of water vapor and exhaled breath via 3D CS@rGO sensor. (b) Sensitivity to humidity for 3D CS@rGO sensor tested with or without 0.1 ppm acetone. (c) Humidity compensation for the acetone vapor sensors in 25%RH, 55%RH, and 85% at room temperature, respectively. Experimental data are shown with linearly fitted dashed line. (d) Response/recovery time values of 3D CS@rGO sensor to 1 ppm acetone under a high relative humidity (85%RH) and room temperature. The error bars display the standard deviation for the three replicates (n=3).

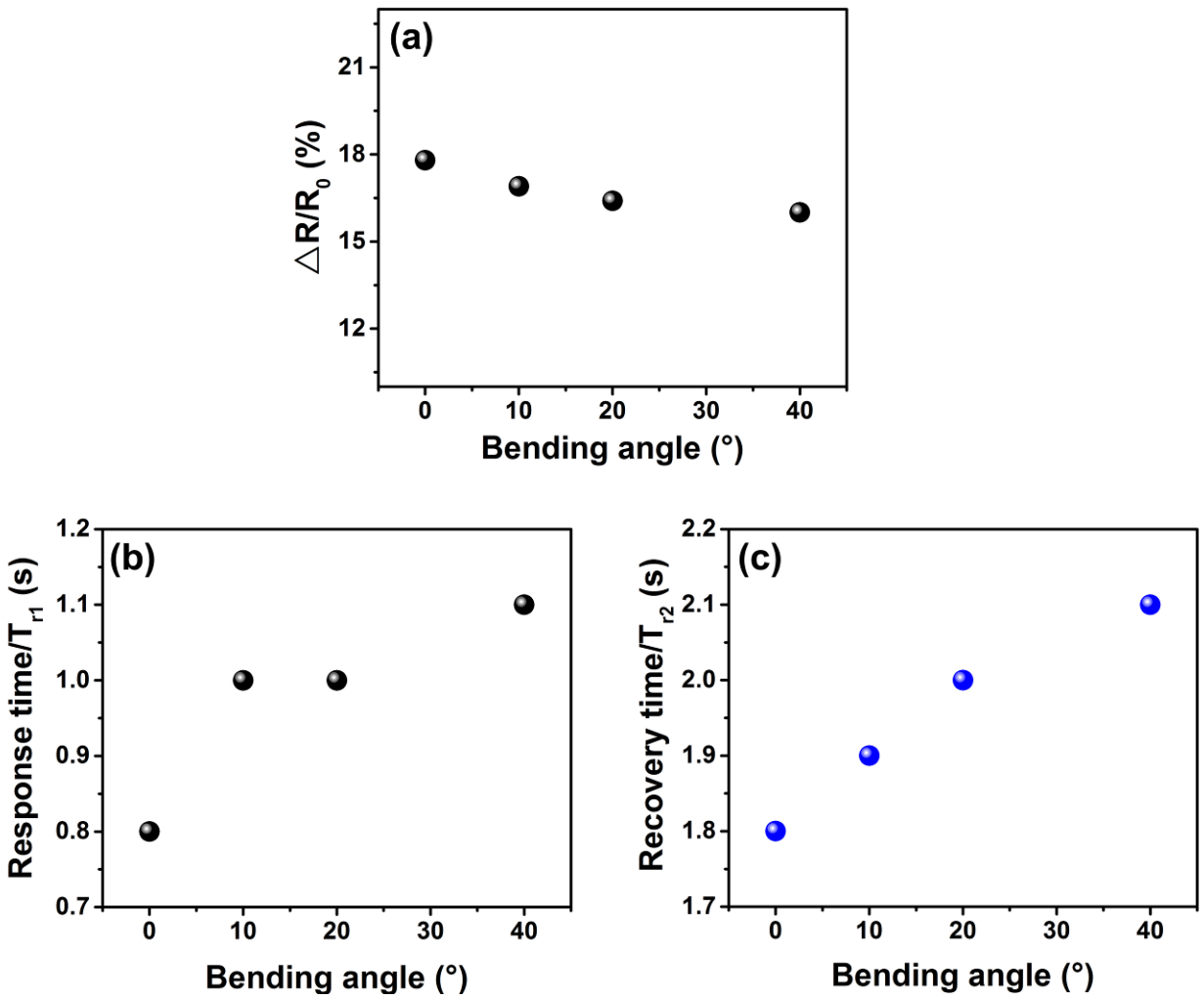

Fig. S11. Mechanical properties and response-recovery characteristic of the 3D CS@rGO sensor. (a) Response values of 3D CS@rGO sensor to 0.5 ppm acetone under various bending angle range from 0° to 40°. (b) Response time and (c) recovery time of 3D CS@rGO sensor to 0.5 ppm acetone under various bending angle range from 0° to 40°.

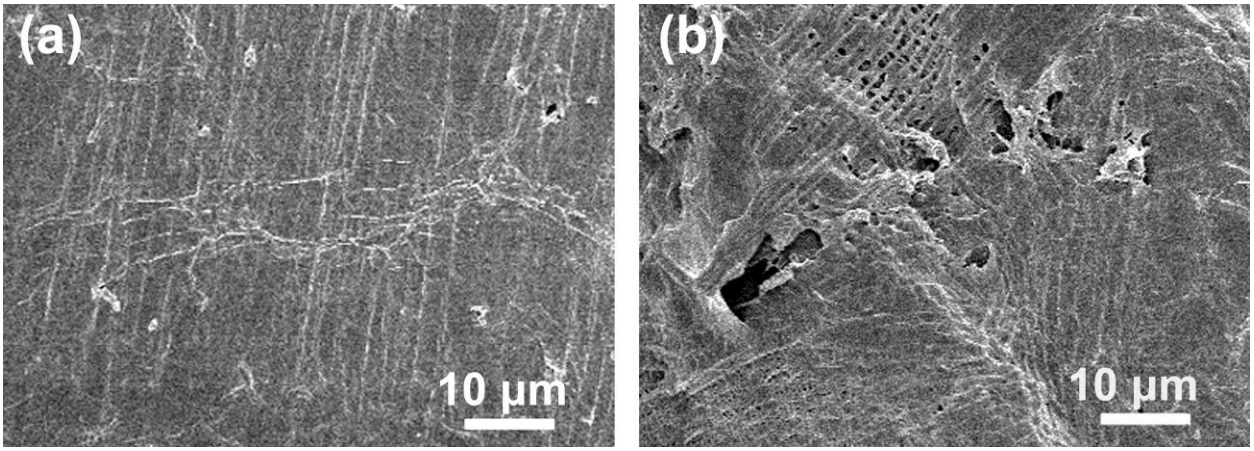

Fig. S12. Low-magnification FESEM images of 3D CS@rGO sensor surface (a) before and (b) after bending.

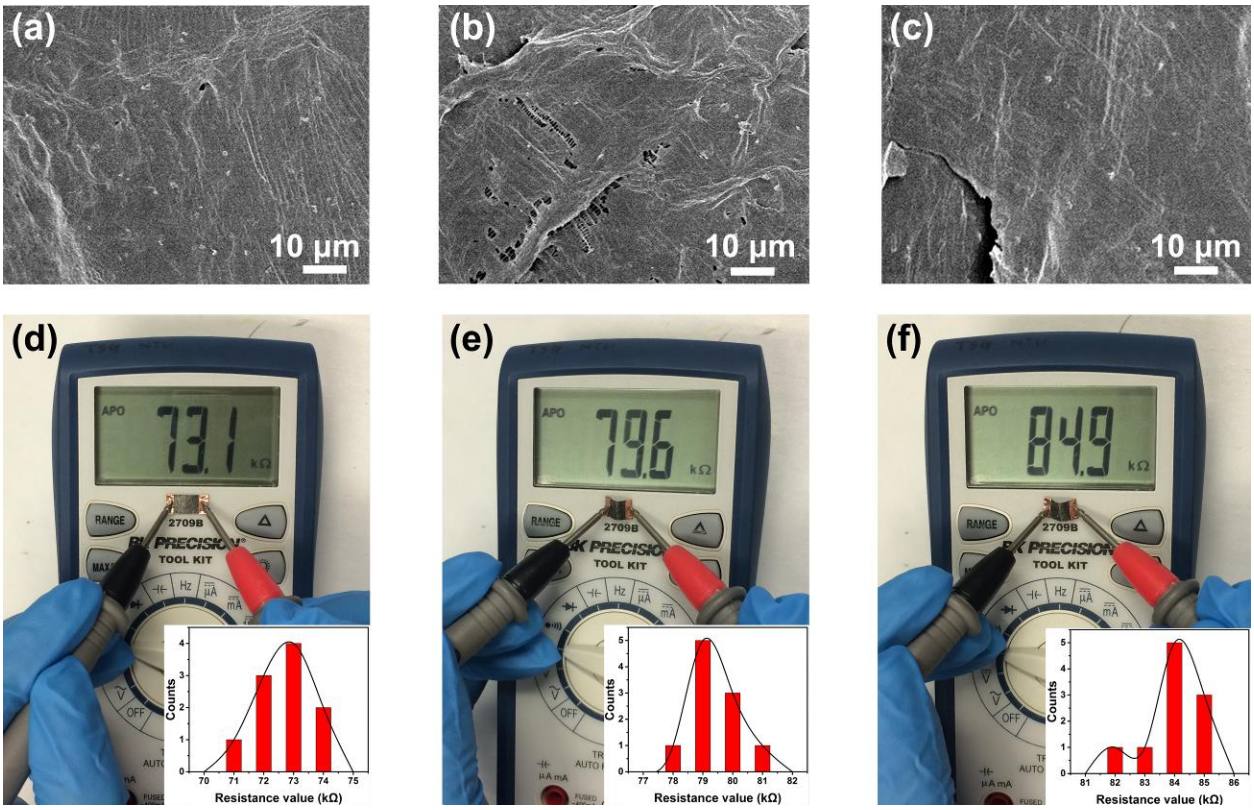

Fig. S13. Mechanical strength properties of the device. (a-c) Low-magnification FESEM images of the 3D CS@rGO sensor surface at its initial condition and after 5 and 10-times of repetitive bending, respectively. (d-f) Resistance values of the 3D CS@rGO sensor before and after the corresponding stress. Inset shows histogram of multiple resistance values obtained at each given condition.

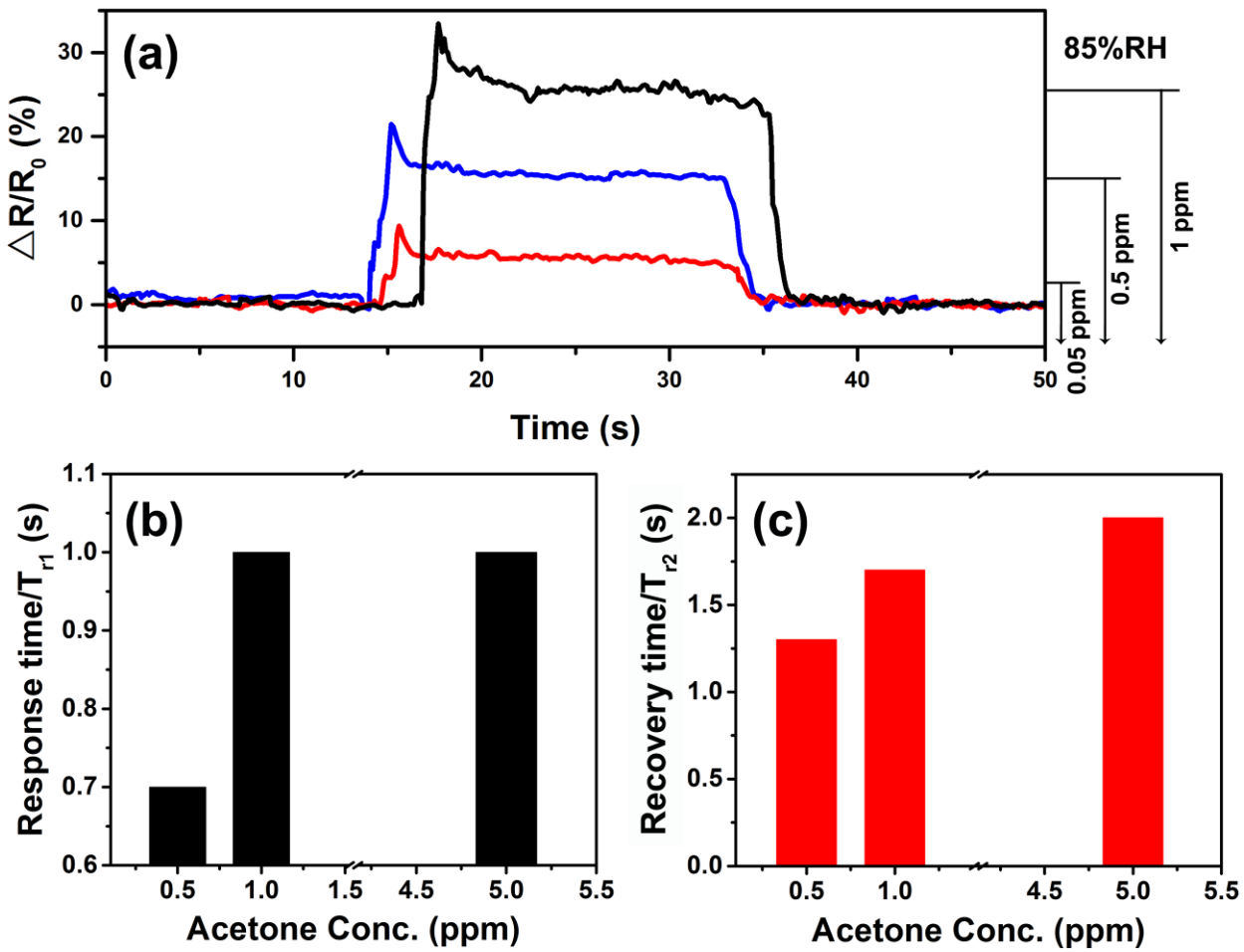

Fig. S14. Sensitivity of 3D CS@rGO with varying acetone concentration under mechanical bending. (a) Sensor response curve to acetone vapors at 0.05 ppm (red), 0.5 ppm (blue), and 1 ppm (black) in 85%RH. (b) Response time values of sensor and (c) recovery time values.

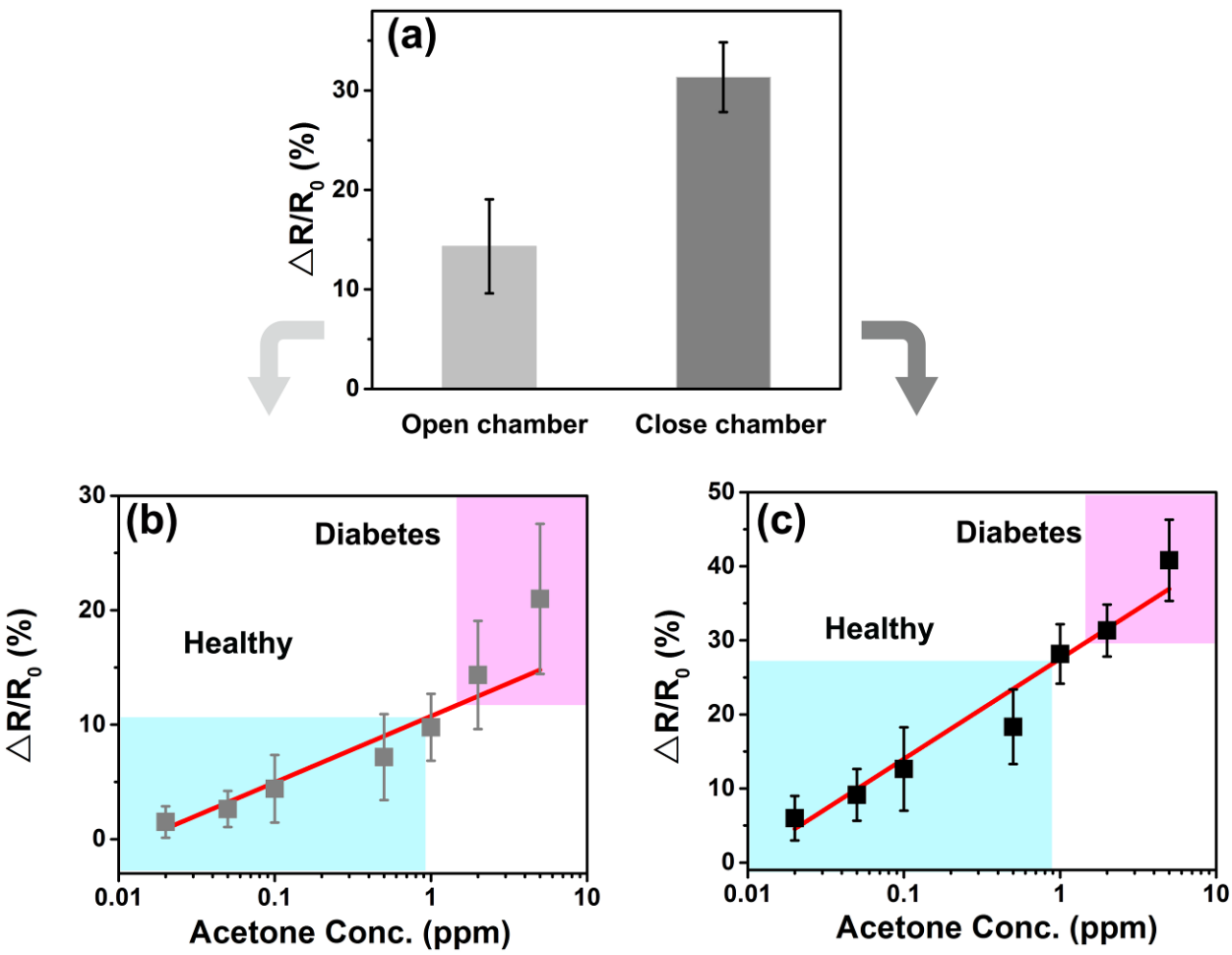

Fig. S15. Calibration for acetone detection scheme using CS@rGO sensor. (a) Sensitivity calibration of 3D CS@rGO sensor under open chamber and close chamber systems. (b) Diabetes-related acetone vapor diagnostic scheme when measurements are performed in open chamber system. (c) Diabetes-related acetone vapor diagnostic scheme when measurements are performed in closed chamber system. The error bars display the standard deviation for the three replicates (N=3).

Table S1. Room temperature acetone-sensing properties of various materials.

Materials	Structure	Detection limit/ppm	Response time/s	Ref.
Chitosan@rGO	3D film	0.02	≤ 1	this work
Chitosan	Smooth film	0.1	10	[9]
Phthalocyanine	Comb film	5	100	[10]
Carbon aerogel	Bulk film	300	100	[11]
Polyaniline	Porous film	229	60	[12]
PVDF-HFP	Porous film	42	450	[13]
SnO_2-rGO	Sphere-based film	10	107	[14]
SnO_2	Porous film	30	30	[15]
V_2O_5	Nanoneedle	0.94	67	[16]

Ref.: References

Table S2. Sensing performances of acetone breath sensors.

Materials	Test ambient	Detection limit/ppm	Working temperature/°C	Response time/s	Ref.
Chitosan@rGO	85%RH	0.02	R.T.	≤ 1	this work
C-WO_3	95%RH	0.9	300	3	[17]
SnO_2	80%RH	0.12	300	11	[18]
Rh-AF-WO_3	90%RH	0.17	350	≤ 20	[1]
Si-WO_3	90%RH	0.2	400	95	[19]
Pt-PS-SnO_2	90%RH	0.01	350	--	[2]
Au-In_2O_3	80%RH	0.02	340	11	[20]
Pt-SnO_2	90%RH	0.025	350	--	[21]
SnO_2@rGO	95%RH	1.0	350	198	[22]
Pt-WO_3	85%RH	0.12	300	≥60	[23]

R.T.: Room temperature; Ref.: References

REFERENCES

1 S. J. Kim, S. J. Choi, J. S. Jang, N. H. Kim, M. Hakim, H. Tuller and I. D. Kim, *ACS Nano*, 2016, **10**, 5891-5899.

2 J. S. Jang, S. J. Choi, S. J. Kim, M. Hakim and I. D. Kim, *Adv. Funct. Mater.*, 2016, **26**, 4740-4748.

3 L. L. Wang, T. Fei, Z. Lou and T. Zhang, *ACS Appl. Mater. Interfaces*, 2011, **3**, 4689-4694.

4 A. Usman, K. M. Zia, M. Zuber, S. Tabasum, S. Rehman and F. Zia, *Int. J. Biol. Macromol*, 2016, **86**, 630-645.

5 W. Suginta, P. Khunkaewla and A. Schulte, *Chem. Rev.*, 2013, **113**, 5458-5479.

6 R. A. Potyrailo, R. K. Bonam, J. G. Hartley, T. A. Starkey, P. Vukusic, M. Vasudev, T. Bunning, R. R. Naik, Z. X. Tang, M. A. Palacios, M. Larsen, L. A. Le Tarte, J. C. Grande, S. Zhong and T. Deng, *Nat. Commun*., 2015, **6**, 12.

7 G. Konvalina and H. Haick, *Acc. Chem. Res.*, 2014, **47**, 66-76.

8 M. Righettoni, A. Tricoli and S. E. Pratsinis, *Chem. Mat.*, 2010, **22**, 3152-3157.

9 T. I. Nasution, I. Nainggolan, S. D. Hutagalung, K. R. Ahmad and Z. A. Ahmad, *Sens. Actuator B*, 2013, **177**, 522-528.

10 A. Rydosz, E. Maciak, K. Wincza and S. Gruszczynski, *Sens. Actuators B*, DOI:10.1016/j.snb.2016.06.168.

11 F. S. Dias, L. G. Tartuci, H. F. Gorgulho and W. S. Machado, *Sens. Actuators B*, 2016, **231**, 440-449.

12 J. S. Do and S. H. Wang, *Sens. Actuators B*, 2013, **185**, 39-46.

13 A. Daneshkhah, S. Shrestha, M. Agarwal and K. Varahramyan, *Sens. Actuators B*, 2015, **221**, 635-643.

14 D. Z. Zhang, A. M. Liu, H. Y. Chang and B. K. Xia, *RSC Adv.*, 2015, **5**, 3016-3022.

15 S. F. Shao, H. Y. Wu, S. M. Wang, Q. L. Hong, R. Koehn, T. Wu and W. F. Rao, *J. Mater. Chem. C*, 2015, **3**, 10819-10829.

16 S. A. Hakim, Y. L. Liu, G. S. Zakharova and W. Chen, *RSC Adv.*, 2015, **5**, 23489-23497.

17 T. Xiao, X. Y. Wang, Z. H. Zhao, L. Li, L. Zhang, H. C. Yao, J. S. Wang and Z. J. Li, *Sens. Actuator B*,. 2014, **199**, 210-219.

18 J. Shin, S. J. Choi, I. Lee, D. Y. Youn, C. O. Park, J. H. Lee, H. Tuller and I.D. Kim, *Adv. Funct. Mater.*, 2013, **23**, 2357-2367.

19 M. Righettoni, A. Tricoli and S. E. Pratsinis, *Anal. Chem.*, 2010, **82**, 3581-3587.

20 R. Q. Xing, Q. L. Li, L. Xia, J. Song, L. Xu, J. H. Zhang, Y. Xie and H. W. Song, *Nanoscale*, 2015, **7**, 13051-13060.

21 J. S. Jang, S. J. Kim, S. J. Choi, N. H. Kim, M. Hakim, A. Rothschild and I. D. Kim, *Nanoscale*, 2015, **7**, 16417-16426.

22 S. J. Choi, B. H. Jang, S. J. Lee, B. M. Min, A. Rothschild and I. D. Kim, *ACS Appl. Mater. Interfaces*, 2014, **6**, 2588-2597.

23 S. J. Choi, I. Lee, B. H. Jang, D. Y. Youn, W. H. Ryu, C. O. Park and I. D. Kim, *Anal. Chem.*, 2013, **85**, 1792-1796.